

Relationship between the heat transfer law and the scalar dissipation function in a turbulent channel flow

Hiroyuki Abe^{1,†} and Robert Anthony Antonia²

¹Japan Aerospace Exploration Agency, Tokyo 182-8522, Japan

²Discipline of Mechanical Engineering, University of Newcastle, Newcastle, New South Wales 2308, Australia

(Received 27 February 2017; revised 26 June 2017; accepted 8 August 2017;
first published online 29 September 2017)

Integration across a fully developed turbulent channel flow of the transport equations for the mean and turbulent parts of the scalar dissipation rate yields relatively simple relations for the bulk mean scalar and wall heat transfer coefficient. These relations are tested using direct numerical simulation datasets obtained with two isothermal boundary conditions (constant heat flux and constant heating source) and a molecular Prandtl number Pr of 0.71. A logarithmic dependence on the Kármán number h^+ is established for the integrated mean scalar in the range $h^+ \geq 400$ where the mean part of the total scalar dissipation exhibits near constancy, whilst the integral of the turbulent scalar dissipation rate $\overline{\varepsilon_\theta}$ increases logarithmically with h^+ . This logarithmic dependence is similar to that established in a previous paper (Abe & Antonia, *J. Fluid Mech.*, vol. 798, 2016, pp. 140–164) for the bulk mean velocity. However, the slope (2.18) for the integrated mean scalar is smaller than that (2.54) for the bulk mean velocity. The ratio of these two slopes is 0.85, which can be identified with the value of the turbulent Prandtl number in the overlap region. It is shown that the logarithmic h^+ increase of the integrated mean scalar is intrinsically associated with the overlap region of $\overline{\varepsilon_\theta}$, established for $h^+ (\geq 400)$. The resulting heat transfer law also holds at a smaller $h^+ (\geq 200)$ than that derived by assuming a log law for the mean temperature.

Key words: turbulence simulation, turbulent boundary layers, turbulent flows

1. Introduction

The transport of heat and mass (i.e. scalar) in wall-bounded turbulent flows has attracted significant attention in the past several decades. In particular, similarity arguments developed for the velocity field have been successfully extended to the scalar field when the molecular Prandtl number Pr is close to unity (see, for example, Monin & Yaglom 1971; Townsend 1976; Kader 1981; Subramanian & Antonia 1981; Nagano & Tagawa 1988). Also, an increased use has been made of direct numerical simulations (DNSs) to understand the underlying physics of turbulence since these provide detailed spatial and temporal information with high accuracy. The seminal

† Email address for correspondence: habe@chofu.jaxa.jp

work by Kim & Moin (1989) dealt with a passive scalar transport in a turbulent channel flow with a Kármán number $h^+ (\equiv U_\tau h/\nu) = 180$ and three values (0.2, 0.71 and 2.0) of the molecular Prandtl number Pr . Here, h^+ represents the ratio of the half-width of the channel h and the viscous length scale ν/U_τ ($U_\tau (\equiv (\tau_w/\rho)^{1/2})$ is the friction velocity, where τ_w is the wall shear stress and ρ is the density of the fluid; the superscript $+$ denotes normalization by wall units). They used an internal heating source so that the passive scalar was created internally and removed from two isothermal walls. Since then, several DNS studies have been performed in a turbulent channel flow with passive scalar transport for higher Reynolds numbers and various thermal boundary conditions (Johansson & Wikström 1999; Kawamura, Abe & Matsuo 1999; Morinishi, Tamano & Nakamura 2003; Abe, Kawamura & Matsuo 2004a; Abe, Antonia & Kawamura 2009; Antonia, Abe & Kawamura 2009; Hasegawa & Kasagi 2011; Saruwatari & Yamamoto 2014; Pirozzoli, Bernardini & Orlandi 2016). In these studies, the functional Re and Pr dependence of mean and turbulence quantities relating to the scalar dissipation function (defined in (1.19)) has been examined intensively. As for the velocity field (Kaneda, Morishita & Ishihara 2013; Lee & Moser 2015), the maximum h^+ in the DNS has increased significantly for the scalar field and is now around 4000 (Pirozzoli *et al.* 2016). It became recently evident that the mean scalar obeys the generalized logarithmic law in the lower half of the channel and a parabolic defect profile in the core region (see Pirozzoli *et al.* 2016).

One of the important quantities to be obtained accurately is the heat transfer coefficient (or equivalently the Stanton number), *viz.*

$$h_t \equiv Q_w/\rho C_p U_b T_m = 1/U_b^+ T_m^+, \tag{1.1}$$

where $Q_w = \rho C_p U_\tau T_\tau$ and C_p are the wall heat flux and specific heat at the constant pressure, respectively; T_τ is the friction temperature. Here, U_b and T_m are the bulk mean velocity and the mixed mean (or sometimes bulk mean) temperature, respectively, defined such that

$$U_b \equiv \frac{1}{h} \int_0^h \bar{U} \, dy \tag{1.2}$$

and

$$T_m \equiv \frac{1}{h} \int_0^h \frac{\bar{U}\bar{\Theta}}{U_b} \, dy. \tag{1.3}$$

The form of h_t is analogous to that of the skin friction coefficient, *viz.*

$$C_f \equiv \tau_w/\frac{1}{2}\rho U_b^2 = 2/U_b^{+2}. \tag{1.4}$$

The perfect analogy between C_f and h_t (i.e. $C_f = 2h_t$) is referred to as the Reynolds analogy.

Significant attention was given to the possible h^+ dependence of C_f on the basis of the mean velocity log law. Recently, Zanoun, Nagib & Durst (2009) observed that the logarithmic skin friction relation

$$U_b^+ = \frac{1}{\kappa} \ln(h^+) - \frac{1}{\kappa} + A \tag{1.5}$$

or, equivalently,

$$\sqrt{\frac{2}{C_f}} = \frac{1}{\kappa} \ln(Re_b \sqrt{C_f}/2\sqrt{2}) - \frac{1}{\kappa} + A \quad (1.6)$$

obtained from the logarithmic law of the wall

$$U^+ = \frac{1}{\kappa} \ln(y^+) + A \quad (1.7)$$

(κ and A denote the von Kármán constant and the additive constant, respectively), with $\kappa = 0.37$ and $A = 3.7$, as obtained by Zanoun, Durst & Nagib (2003) represents more accurately the experimental skin friction data than Dean's (1978) formula,

$$C_f = 0.073 Re_b^{-1/4}, \quad (1.8)$$

in particular, for $h^+ > 2000$ (see figure 5 of their paper).

Likewise, a possible h^+ dependence of h_t was examined on the basis of scalar log law. Monin & Yaglom (1971) (see also Kader & Yaglom (1972)) assumed that the logarithmic defect laws for both velocity and scalar are valid up to channel/pipe centreline and obtained a relation for the mixed mean scalar with respect to the Reynolds number, i.e.

$$T_m = \alpha \ln(Re_b \sqrt{C_f}) + \gamma(Pr), \quad (1.9)$$

where α and γ are constants and Re_b denotes the Reynolds number based on U_b and the channel/pipe width. Kader & Yaglom (1972) examined the experimental data in a channel, pipe and boundary layer and noted that $\alpha (= 2.12)$ is independent of Pr and the product of the turbulent Prandtl number $Pr_t (= 0.85)$ and $1/\kappa (= 0.4)$ while γ depends on Pr . They also tested the resulting heat transfer coefficient h_t , i.e.

$$h_t = \frac{\sqrt{(C_f/2)}}{\alpha \ln(Re_b \sqrt{C_f}) + \gamma(Pr)}, \quad (1.10)$$

in a pipe flow for $Pr = 0.71$ against large amount of experimental data. They stated that the agreement with the experimental data is excellent except for $Re_b < 2 \times 10^4$ ($R^+ < 500-600$) where the well-known power-law relation of Kays (1966) given by

$$h_t = 0.018 Re_b^{-0.2} Pr^{-0.5} \quad (1.11)$$

fits the data slightly better than (1.10) (see also figure 2 of their paper).

On the other hand, a different approach can be taken for establishing possible h^+ dependences for both C_f and h_t with the use of energy balances for both mean and turbulent parts (i.e. via a global energy balance). In this context, Abe & Antonia (2016) examined the relationship between the skin friction coefficient C_f and the energy dissipation function E (Rotta 1962), consisting of mean and turbulent parts, i.e.

$$E \equiv \underbrace{\nu \overline{u_{i,j}(u_{i,j} + u_{j,i})}}_{\bar{\varepsilon}} + \underbrace{\nu \overline{U_{i,j}(\overline{U}_{i,j} + \overline{U}_{j,i})}}_{\bar{\varepsilon}_{mean}}, \quad (1.12)$$

using their DNS database in a turbulent channel flow together with other DNS and experimental data up to $h^+ = 10^4$. Note that u_1, u_2, u_3 denote the streamwise,

wall-normal and spanwise velocity fluctuations, respectively; u , v , w are used interchangeably with u_1 , u_2 , u_3 ; ν denotes the kinematic viscosity and the overbar denotes averaging with respect to x , z (x , y , z are the streamwise, wall-normal and spanwise directions, respectively) and t (time); upper cases denote instantaneous quantities. Given that the total energy dissipated in the channel is equal to the energy input via the mean pressure gradient, the energy balance was given by

$$E = -\frac{1}{\rho} \frac{d\bar{P}}{dx} U_b h = U_\tau^2 U_b \quad \text{or equivalently,} \quad U_b^+ = E/U_\tau^3. \quad (1.13a,b)$$

It was noted that the logarithmic skin friction law, established on the basis of (1.13), viz.

$$U_b^+ (\equiv U_b/U_\tau) = 2.54 \ln(h^+) + 2.41, \quad (1.14)$$

or, equivalently,

$$\frac{1}{\sqrt{C_f}} = 1.80 \ln(Re_b \sqrt{C_f}) - 0.163, \quad (1.15)$$

was shown to hold reasonably well over a wider range of h^+ (i.e. $300 \leq h^+ \leq 10^4$) than that based on the velocity log law. It was also noted that the logarithmic h^+ dependence of (1.14) is essentially associated with the overlap scaling of $\bar{\varepsilon}$ even at small h^+ .

Here, we extend the scope of the work by Abe & Antonia (2016) to a passive scalar field. In this context, Pirozzoli *et al.* (2016) investigated global energy balances for both streamwise velocity and scalar with a constant heating source (CHS) with their DNS datasets. Their isothermal boundary condition leads to a nearly perfect analogy between the Navier–Stokes and scalar conservation equations. The resulting scalar energy balance is written as

$$E_S = QhT_b \quad \text{or equivalently,} \quad T_b^+ = E_S/U_\tau T_\tau^2, \quad (1.16a,b)$$

where the heat source

$$Q = Q_w/\rho C_p h = U_\tau T_\tau/h \quad (1.17)$$

and the integrated mean scalar

$$T_b \equiv (1/h) \int_0^h \bar{\Theta} \, dy. \quad (1.18)$$

Note that T_b is used instead of T_m owing to the given thermal boundary condition. Like E , the scalar energy dissipation function E_S consists of mean and turbulent parts, i.e.

$$E_S \equiv \underbrace{a\overline{\theta_j^2}}_{\bar{\varepsilon}_\theta} + \underbrace{a\overline{\Theta_{,j}^2}}_{\bar{\varepsilon}_\theta \text{ mean}} \quad (1.19)$$

(a is the thermal diffusivity). Pirozzoli *et al.* (2016) reported a $\ln(h^+)$ dependence for both U_b^+ and T_b^+ for $Pr = 1$ in the range $550 \leq h^+ \leq 4000$ where there is a discernible difference between U_b^+ and T_b^+ and the rate of increase is slightly larger for U_b^+ than for T_b^+ . They also noted that the $\ln(h^+)$ dependence of both U_b^+ and T_b^+ is associated with the turbulent dissipation parts and inferred that the latter terms are expected to dominate in the asymptotic high- Re regime. It is however not clear whether the $\ln(h^+)$ dependence of E_S is intimately associated with the overlap region

of the turbulent dissipation part, as was previously established for E (Abe & Antonia 2016), and whether the resulting logarithmic relation of h_t extends to a lower Reynolds number than that for which the velocity and scalar log laws hold (*viz.* equation (1.10)). The association with the overlap region (approximately between $y^+ = 30$ and $y/h = 0.2$) is important since this region holds the key to understanding high Reynolds number turbulent flows. This is the main theme of the present work, which uses the DNS database of a turbulent channel flow with passive scalar transport for $Pr = 0.71$ (Abe *et al.* 2004a, 2009); the present results are compared with those from other DNS data (Kim & Moin 1989; Horiuti 1992; Kasagi, Tomita & Kuroda 1992; Morinishi *et al.* 2003; Tsukahara *et al.* 2006; Hasegawa & Kasagi 2011; Pirozzoli *et al.* 2016) up to $h^+ = 4000$.

Attention is also given to the effects associated with different thermal boundary conditions since, as indicated by Pirozzoli *et al.* (2016), there is a discernible difference in the mean temperature distributions between two analogous isothermal boundary conditions (i.e. a constant heating source (Pirozzoli *et al.* 2016) and constant heat flux (CHF) (Abe *et al.* 2004a) (see also §2)) in the core part of the channel. This difference is likely to affect the extent of the overlap region for the scalar field. Possible effects of these two thermal boundary conditions are however yet to be examined in detail, in particular, regarding quantities associated with E_S . This issue is also pursued in the present work.

This paper is organized as follows. In §2, the expression for the total scalar energy dissipation function E_S is obtained by integrating the transport equations for the mean and turbulent parts of the scalar dissipation for two isothermal conditions (i.e. CHS and CHF). Following a brief description of the present DNS databases in §3 and after clarifying the degree of similarity between CHF and CHS in §4.1, results for the h^+ dependence of E_S are given in §4.2 and discussed in the context of available data for the dependence on h^+ of the integrated mean and turbulent scalar dissipation rates. In §§4.3 and 4.4, we focus on the scaling laws of the turbulent scalar dissipation rate $\overline{\varepsilon_\theta}$ and provide an explanation for the $\ln(h^+)$ dependence of E_S . Conclusions are given in §5.

2. Relation for the scalar dissipation function

In this paper, we consider two heating conditions. One is CHS, which was first used by Kim & Moin (1989). In this condition, the similarity between the scalar conservation and Navier–Stokes equations is convincing (except for the pressure-gradient term in the latter equation) when $Pr = 1$. The other is CHF proposed by Kasagi *et al.* (1992) who noted that the constant heating source would be difficult to set up experimentally (see also Teitel & Antonia 1993). In each case, the wall is kept isothermal and the temperature fluctuation is assumed to be zero at the two walls.

Here we assume that the fluid is hot whereas the two walls are cold (i.e. $T = -\Theta$). The normalized scalar conservation equation is then given by

$$\frac{\partial \Theta}{\partial t} + U_j \frac{\partial \Theta}{\partial x_j} = a \frac{\partial^2 \Theta}{\partial x_j^2} + Q. \quad (2.1)$$

For CHS, the temperature is created internally and removed from both walls (i.e. equation (1.17)). For CHF, it is required that the mixed mean temperature T_m , defined in (1.3), increases linearly with x , i.e.

$$T = \frac{\partial \tilde{T}_m}{\partial x} x - \Theta, \quad (2.2)$$

where the tilde denotes averaging with respect to z and t . This first term on the right-hand side of (2.2) can be written as

$$\frac{\partial \tilde{T}_m}{\partial x} = \frac{\partial \tilde{T}_w}{\partial x} = \frac{2Q_w}{\rho C_p \int_0^{2h} \bar{U} dy}. \tag{2.3}$$

Energy balance then leads to a relation

$$Q = U \frac{\partial \tilde{T}_m}{\partial x} \quad \text{or equivalently,} \quad Q = \frac{2Q_w U}{\rho C_p \int_0^{2h} \bar{U} dy}. \tag{2.4a,b}$$

In a channel flow, a relation for the total scalar dissipation E_S is obtained readily using the total heat flux relation, viz.

$$Q_{total} \equiv -\overline{v\theta} + a \frac{d\bar{\Theta}}{dy} = \left(\frac{Q_w}{\rho C_p} - yQ \right). \tag{2.5}$$

By multiplying (2.5) by $d\bar{\Theta}/dy$, we obtain the mean energy balance for the scalar field, viz.

$$-\overline{v\theta} \frac{d\bar{\Theta}}{dy} + a \left(\frac{d\bar{\Theta}}{dy} \right)^2 = \left(\frac{Q_w}{\rho C_p} \frac{d\bar{\Theta}}{dy} - yQ \frac{d\bar{\Theta}}{dy} \right). \tag{2.6}$$

$(Q_w/\rho C_p)(d\bar{\Theta}/dy)$ represents the rate of energy transfer from the outer part of the boundary layer to the inner region; the term which includes Q is the energy input from the heat source. Part of the energy is dissipated directly by thermal diffusivity (the second term on the left of (2.6)), whilst the rest is extracted to turbulence via the work done by the wall-normal turbulent heat flux (the first term on the left of (2.6)).

On the other hand, the transport equation for scalar variance $k_\theta (\equiv \overline{\theta^2}/2)$ is written as

$$P_\theta - \frac{1}{2} \frac{d}{dy} (\overline{\theta^2 v}) + \frac{a}{2} \frac{d^2}{dy^2} (\overline{\theta^2}) - \overline{\varepsilon_\theta} = 0, \tag{2.7}$$

where

$$P_\theta = -\overline{v\theta} \frac{d\bar{\Theta}}{dy}. \tag{2.8}$$

While CHF leads to an additional term for (2.8), i.e. $\overline{u\theta}(\partial \tilde{T}_w/\partial x)$, its magnitude is negligibly small (see Kasagi *et al.* 1992) and thus this term can be omitted in (2.8). Relation (2.8) is identical with the first term of (2.6), indicating that the energy extracted from the mean field is used for the production for the turbulent field. Integrating (2.7) across the half-channel leads to a relation,

$$\langle P_\theta \rangle = \langle \overline{\varepsilon_\theta} \rangle. \tag{2.9}$$

Relation (2.9) implies that the total production of the scalar variance is balanced by the scalar dissipation rate.

The mean energy balance (i.e. equation (2.6)) can thus be written, after some algebra, as

$$-\frac{\overline{v\theta}}{\overline{v\theta}} \frac{d\overline{\Theta}}{dy} + a \left(\frac{d\overline{\Theta}}{dy} \right)^2 = u_\tau T_\tau \frac{d\overline{\Theta}}{dy} \left(1 - \frac{y}{h} \right) \quad (2.10)$$

and

$$-\frac{\overline{v\theta}}{\overline{v\theta}} \frac{d\overline{\Theta}}{dy} + a \left(\frac{d\overline{\Theta}}{dy} \right)^2 = u_\tau T_\tau \frac{d\overline{\Theta}}{dy} \left(1 - \frac{\int_0^y U dy}{U_b} \right) \quad (2.11)$$

for CHS and CHF, respectively. By assuming symmetry with respect to the centreline, integrating (2.10) and (2.11) across the half-channel then yields relations, in normalized forms, for the total scalar dissipation E_S , i.e.

$$E_S/U_\tau T_\tau^2 \equiv \langle \overline{\varepsilon_\theta} \rangle / U_\tau T_\tau^2 + \left\langle a \left(\frac{d\overline{\Theta}}{dy} \right)^2 \right\rangle / U_\tau T_\tau^2 = T_b/T_\tau \quad (2.12)$$

and

$$E_S/U_\tau T_\tau^2 \equiv \langle \overline{\varepsilon_\theta} \rangle / U_\tau T_\tau^2 + \left\langle a \left(\frac{d\overline{\Theta}}{dy} \right)^2 \right\rangle / U_\tau T_\tau^2 = T_m/T_\tau \quad (2.13)$$

for CHS and CHF (the angular brackets denote integration with respect to y across the channel half-width). Relation (2.12) is the same as that obtained in Pirozzoli *et al.* (2016) in their global energy balance (see relation (3.12) of their paper). Importantly, h^+ does not appear explicitly in these two relations.

In (2.12) and (2.13), the total scalar dissipation E_S contains contributions from the turbulent and viscous dissipation parts. The latter and former should dominate near the wall and in the outer region, respectively. Since the viscous contribution is unlikely to depend on h^+ when the latter is sufficiently large, one expects the dependence on h^+ of the integrated mean scalar (T_b/T_τ and T_m/T_τ) which is related to the heat transfer coefficient h_t , to reflect that of $\langle \overline{\varepsilon_\theta} \rangle$. This will be discussed further in § 4, mainly in the context of the present and available DNS datasets.

3. DNS databases

The present numerical databases have been obtained from DNSs in a turbulent channel flow with passive scalar transport by Abe *et al.* (2004a) and Abe *et al.* (2009). The present flow is a fully developed turbulent channel flow driven by a constant streamwise mean pressure gradient. Four values of h^+ ($= 180, 395, 640$ and 1020) are used. CHF is considered as a thermal boundary condition. The working fluid is air (*viz.* $Pr = 0.71$). We also compare with our unpublished data ($h^+ = 180, 395$ and 640) for CHS and other DNS data available in the literature up to $h^+ = 4000$ (Kim & Moin 1989; Horiuti 1992; Kasagi *et al.* 1992; Morinishi *et al.* 2003; Tsukahara *et al.* 2006; Hasegawa & Kasagi 2011; Pirozzoli *et al.* 2016).

The numerical methodology for the DNSs is briefly as follows. A fractional step method is used with semi-implicit time advancement. The third-order Runge–Kutta method is used for the viscous terms in the y direction and the Crank–Nicolson method is used for the other terms. A finite difference method is adopted for the spatial discretization. A fourth-order central scheme is used in the x and z directions,

whilst a second-order central scheme is used in the y direction. The periodic boundary condition is employed in the x and z directions, whereas the no-slip condition applies in the y direction. For the flow field, all the variables have been normalized by the friction velocity $U_\tau (\equiv \sqrt{\tau_w/\rho})$ and channel half-width h . U_τ is obtained from the mean momentum balance, i.e.

$$\tau_w = -h \frac{d\bar{P}}{dx}. \tag{3.1}$$

For the scalar field, they are non-dimensionalized by the friction velocity U_τ , friction temperature $T_\tau (\equiv Q_w/\rho C_p U_\tau)$ and channel half-width h . T_τ is inferred from the mean scalar balance (i.e. equation (1.17)). Further details on the simulations are given in Abe, Kawamura & Matsuo (2001), Abe *et al.* (2004a,b, 2009) and Antonia *et al.* (2009), and the reader may refer to these papers for information on basic turbulence statistics.

The computational domain size ($L_x \times L_y \times L_z$), number of grid points ($N_x \times N_y \times N_z$) and spatial resolution ($\Delta x, \Delta y, \Delta z$) are given in table 1, the superscript * representing normalization by either $v_K (\equiv (\nu\bar{\epsilon})^{1/4})$; the Kolmogorov velocity scale) or $\eta (\equiv (\nu^3/\bar{\epsilon})^{1/4})$; the Kolmogorov length scale); the subscripts w and c referring to the wall and centreline, respectively. The effect of the domain size was examined by Abe, Kawamura & Choi (2004b) ($h^+ = 640$) who compared two cases: ($L_x \times L_z$) = ($6.4h \times 2h$) and ($12.8h \times 6.4h$). They found that the effect on the mean flow variables and second-order moments was negligible. Abe & Antonia (2016) also examined possible effects of the streamwise domain size L_x on the total dissipation function E . They noted that while a relatively long channel is required for the experiment to achieve a fully developed flow condition (i.e. $d\bar{P}/dx = \text{const.}$) (Monty (2005) suggests $L = 260h$), the accurate determination of τ_w in the DNS requires the channel length to be $L_x \geq 2\pi h$, which supports the finding of Lozano-Durán & Jiménez (2014) that $L_z = 2\pi h$ is sufficient to obtain good one-point statistics up to the centre of the channel.

Since the degree of similarity/dissimilarity between CHF and CHS is yet to be addressed in detail, we examine this issue in §4.1 on the main quantities of interest, *viz.* those which contribute mostly to E_s . This will be done by comparing the present simulations with the two thermal boundary conditions for $h^+ = 180, 395$ and 640 . Note that we run simulations with two different thermal boundary conditions simultaneously with the same domain size, number of grid points and spatial resolutions listed in table 1.

4. Results for the scalar dissipation function and heat transfer coefficient

4.1. Constant heat flux versus constant heating source

We first examine the degree of similarity between CHF and CHS on quantities associated with E_s . Figure 1 shows distributions of the normalized mean scalar $\bar{\Theta}/T_\tau$ (or equivalently $\bar{\Theta}^+$), the dissipation associated with the mean scalar $a(d\bar{\Theta}/dy)^2 \nu/U_\tau^2 T_\tau^2$ (or equivalently $(d\bar{\Theta}^+/dy^+)^2/Pr$), the wall-normal turbulent heat flux $-\overline{v\theta}/U_\tau T_\tau$ (or equivalently $-\overline{v^+\theta^+}$) and the production term $P_\theta \nu/U_\tau^2 T_\tau^2$ (or equivalently P_θ^+) for $Pr = 0.71$. In figure 1(a), the empirical relation of Kader (1981) is also plotted. While the logarithmic law

$$\bar{\Theta}^+ = \frac{1}{\kappa_\theta} \ln y^+ + A_\theta \tag{4.1}$$

with a von Kármán constant for the mean scalar $\kappa_\theta = 0.43$ and an additive constant $A_\theta = 3.0$ provides a good fit to the DNS data for $h^+ = 1020$ (see figure 1a), the value

	180	395	640	1020
h^+				
$L_x \times L_y \times L_z$		$12.8h \times 2h \times 6.4h$		
$L_x^+ \times L_y^+ \times L_z^+$	$2304 \times 360 \times 1152$	$5056 \times 790 \times 2528$	$8192 \times 1280 \times 4096$	$13\,056 \times 2040 \times 6528$
$N_x \times N_y \times N_z$	$768 \times 128 \times 384$	$1536 \times 192 \times 768$	$2048 \times 256 \times 1024$	$2048 \times 448 \times 1536$
$\Delta x^+, \Delta y^+, \Delta z^+$	$3.00, 0.20-5.90, 3.00$	$3.29, 0.15-6.52, 3.29$	$4.00, 0.15-8.02, 4.00$	$6.38, 0.15-7.32, 4.25$
$\Delta x_w^*, \Delta y_w^*, \Delta z_w^*$	$1.94, 0.13, 1.94$	$2.24, 0.10, 2.24$	$2.77, 0.11, 2.77$	$4.46, 0.11, 2.97$
$\Delta x_c^*, \Delta y_c^*, \Delta z_c^*$	$0.82, 1.62, 0.82$	$0.74, 1.47, 0.74$	$0.82, 1.64, 0.82$	$1.16, 1.33, 0.77$

TABLE 1. Domain size, grid points and spatial resolution of the DNS databases. Constant heat flux case covers $h^+ = 180-1020$, whereas constant heating source case covers $h^+ = 180-640$.

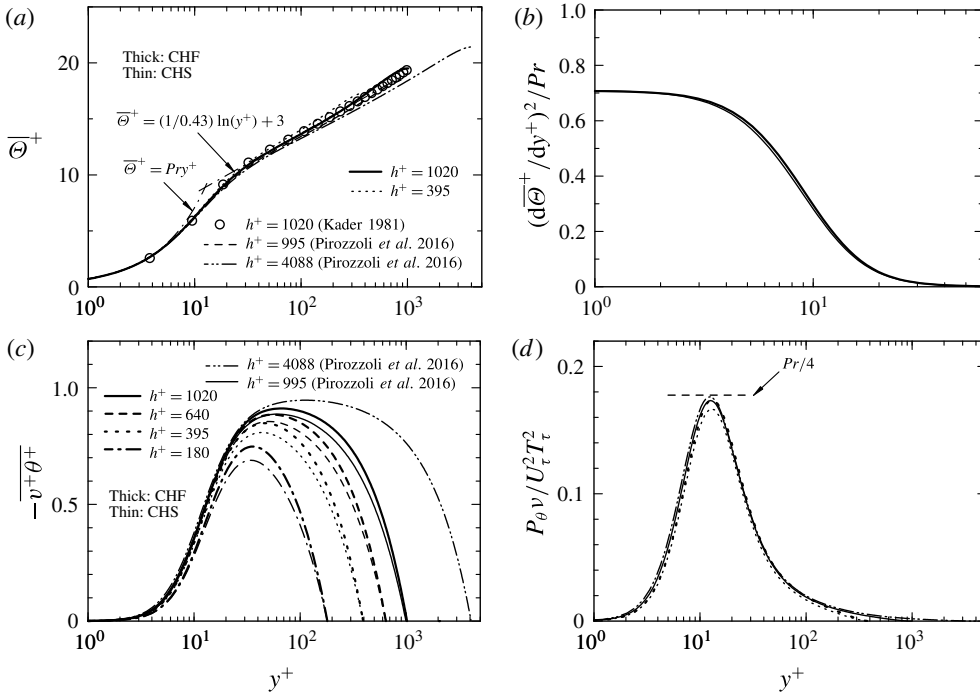


FIGURE 1. Distributions of $\bar{\Theta}^+$, $(d\bar{\Theta}^+/dy^+)^2/Pr$, $-\overline{v^+\theta^+}$ and $P_\theta v/U_\tau^2 T_\tau^2$ for $Pr = 0.71$: (a) $\bar{\Theta}^+$; (b) $(d\bar{\Theta}^+/dy^+)^2/Pr$; (c) $-\overline{v^+\theta^+}$; (d) $P_\theta v/U_\tau^2 T_\tau^2$.

of κ_θ tends to increase slowly with h^+ for $h^+ < 4000$ (see also figure 12 and the more critical examination of the log law in §4.4). The log law is most likely established for the largest h^+ (>4000). There is also a slight difference in the magnitude of $\bar{\Theta}^+$ between CHF and CHS. This difference is pronounced in the core region, in which the empirical relation of Kader (1981) is closer to $\bar{\Theta}^+$ for CHF than for CHS, as noted by Pirozzoli *et al.* (2016). The magnitude of $a(d\bar{\Theta}/dy)^2 v/U_\tau^2 T_\tau^2$ (see figure 1b) is hence slightly greater for CHF than for CHS. The magnitude of $-\overline{v\theta}/U_\tau T_\tau$ is also larger for CHF than for CHS (figure 1c). These results imply a more effective heating for CHF than for CHS. Distributions of P_θ (i.e. the product of $-\overline{v\theta}$ and $d\bar{\Theta}/dy$) normalized by $U_\tau^2 T_\tau^2/\nu$ thus exhibit a discernible difference between the two thermal boundary conditions (figure 1d). In contrast to CHS, the peak value of P_θ for CHF reaches the theoretical maximum value of $Pr/4$ when h^+ is larger than 395 (figure 1d), i.e. the scalar field for CHF reaches a local equilibrium state at a smaller h^+ than for CHS. Since $\langle P_\theta \rangle = \langle \bar{\varepsilon}_\theta \rangle$ (see (2.9)), the difference in the magnitude of P_θ between CHS and CHF cannot be dismissed when considering the magnitude of the total scalar dissipation rate E_S (see §4.2).

Whilst the two heating conditions lead to different magnitudes of mean and turbulent scalar quantities when normalized by either the wall heat flux Q_w or the friction temperature T_τ , the underlying turbulent scalar transport mechanism is essentially the same for CHS and CHF (see figure 2a,b which show the quadrant analysis of $\overline{v\theta}$ and its probability for $h^+ = 640$). The turbulent Prandtl number Pr_t defined as the ratio of turbulent eddy viscosity ν_t ($\equiv \overline{uv}/d\bar{U}/dy$) to turbulent eddy

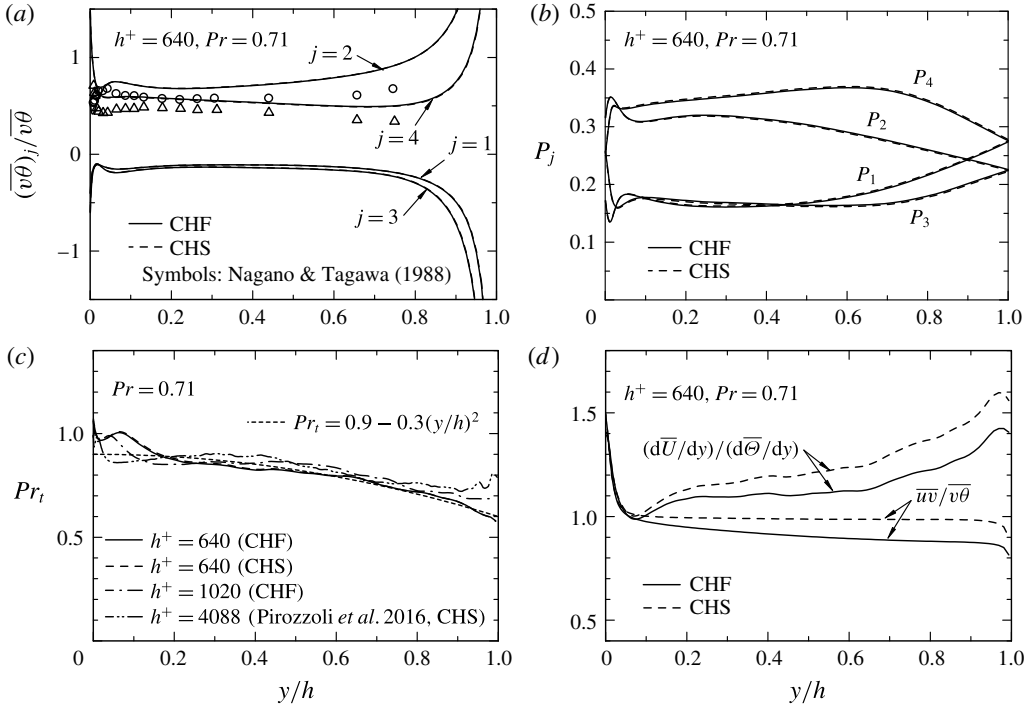


FIGURE 2. Quadrant analysis of $\overline{v\theta}$, its probability P_j and distributions of Pr_t , $(d\overline{U}/dy)/(d\overline{\Theta}/dy)$ and $\overline{uv}/\overline{v\theta}$ for $Pr = 0.71$ as a function of y/h : (a) $(\overline{v\theta})_j / \overline{v\theta}$; (b) P_j ; (c) Pr_t ; (d) $(d\overline{U}/dy)/(d\overline{\Theta}/dy)$ and $\overline{uv}/\overline{v\theta}$.

diffusivity a_t ($\equiv \overline{v\theta}/d\overline{\Theta}/dy$), viz.

$$Pr_t = \frac{v_t}{a_t} = \frac{\overline{uv}}{\overline{v\theta}} \frac{d\overline{\Theta}/dy}{d\overline{U}/dy}, \tag{4.2}$$

is also identical for the two isothermal boundary conditions (see figure 2c). For $y/h > 0.2$, the distributions of Pr_t are described approximately by

$$Pr_t = 0.9 - 0.3(y/h)^2 \tag{4.3}$$

(Abe & Antonia 2009), which is analogous to the relation proposed by Rotta (1962) in a turbulent boundary layer (see also Simpson, Whitten & Moffat 1970). Other DNS data (Kozuka, Seki & Kawamura 2009) also indicate that (4.3) seems to apply not only for air but also for water (viz. $Pr = 5-7$). In the logarithmic region and the lower part of the outer region ($y^+ > 100$ and $y/h < 0.4$), Pr_t is nearly constant (about 0.85), where the magnitudes of $v_t/U_\tau h$ and $a_t/U_\tau h$, which are important measures of the momentum transport and scalar transport respectively, increase monotonically (the distributions of $v_t/U_\tau h$ and $a_t/U_\tau h$ are not shown here) and they are in the range $v_t/U_\tau h = 0.06-0.08$ and $a_t/U_\tau h = 0.08-0.1$ (the Prandtl number dependence is negligibly small when Pr is not far from unity (see Kim & Moin 1989)). The latter two values agree reasonably well with model constants of the two-equation model (i.e. C_μ and C_λ) proposed by Nagano & Kim (1988). For $y/h > 0.4$, the magnitude

of Pr_t decreases gradually to approximately 0.6 at the channel centreline. This is most likely due to the mean scalar gradient being smaller than the mean velocity gradient (see figure 2*d*). In this context, for a DNS with a constant temperature difference (i.e. both isothermal walls are either heated or cooled, so that there is a constant difference in mean temperature between the two walls) (Lyons, Hanratty & McLaughlin 1991; Seki, Abe & Kawamura 2003), the largest mean scalar gradient occurs at the centreline; in this case, Pr_t increases towards the channel centre. The importance of the mean scalar gradient was also suggested for homogeneous shear flows by Rogers, Mansour & Reynolds (1989). They showed that the magnitude of Pr_t increases when the alignment between the turbulent heat flux and mean scalar gradient is perfect. The implication of the present results is that, like the similarity between \mathbf{q} (the fluctuating velocity vector) and θ (see Antonia *et al.* (2009)), the presence of a source (production) term is an important ingredient for a close analogy between the velocity and scalar transport. The difference in magnitude between $d\bar{U}/dy$ and $d\bar{\theta}/dy$ will also be discussed in §4.4 in the context of the von Kármán constants κ and κ_θ .

Note that the decreasing magnitude of Pr_t is essentially associated with the unmixedness of the scalar (Guezennec, Stretch & Kim 1990; Antonia *et al.* 2009; Pirozzoli *et al.* 2016). Here, close inspection of instantaneous fields has further revealed that negative regions of θ are more significantly transported than those of u by vortical motions in the outer region (see also the relationship between the vorticity and scalar derivative vectors in Abe *et al.* (2009)), leading to an increased dissimilarity between velocity and scalar transports (see, for example, $y/h \approx 0.8$ and $z/h \approx 1.5$ in figure 3). In the latter context, Djenidi & Antonia (2009) also noted that, for a three-dimensional transitional wake of a heated square cylinder, the passive scalar is more effectively transported by vortical motions than momentum except close to the cylinder where the magnitudes of the mean velocity and scalar gradients are large. The enhanced scalar transport by vortical motions is most likely responsible for the decrease of Pr_t towards the centreline. This may also explain the difference in scaling behaviours between \overline{uu} and $\overline{\theta\theta}$; the collapse of $\overline{\theta\theta}/T_\tau^2$ is more convincing than that of \overline{uu}/U_τ^2 in the outer region (Pirozzoli *et al.* 2016) where a mixed scaling, or normalization by $U_\tau U_0$ (U_0 is the mean centreline velocity), seems to yield an adequate collapse for \overline{uu} (Bernardini, Pirozzoli & Orlandi 2014).

4.2. Scalar integrals and their Reynolds number dependence

Next, attention is given to the h^+ dependence of the total scalar dissipation function $E_S/U_\tau T_\tau^2$, hence T_m^+ for CHF (2.13) or T_b^+ for CHS (2.12). Distributions of T_m and T_b , normalized by T_τ are given in figures 4(*a*) and (*b*), respectively, as a function of h^+ . Clearly, the magnitudes of both T_m^+ and T_b^+ increase logarithmically with increasing h^+ when h^+ exceeds 400. This increase is described well by

$$T_m^+ = 2.18 \ln(h^+) + 2.40 \tag{4.4}$$

and

$$T_b^+ = 2.18 \ln(h^+) + 1.30 \tag{4.5}$$

for CHF and CHS, respectively. While the slope for T_m^+ (4.4) is close to that obtained by Kader & Yaglom (1972) for a pipe flow (see figure 4(*a*) where the CHF pipe data of Ould-Rouiss, Bousbai & Mazouz (2013) are also plotted), the intercept is somewhat smaller than for the channel. Figure 4 underlines that the slope of 2.18

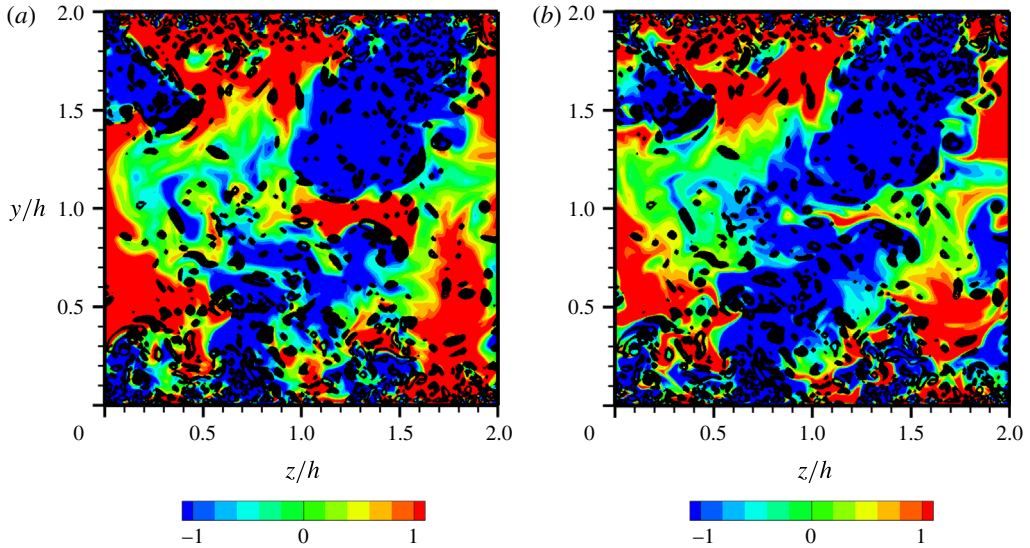


FIGURE 3. Instantaneous isocontours in the y - z plane of the streamwise velocity and scalar fluctuations for $h^+ = 1020$: (a) u^+ ; (b) θ^+ for $Pr = 0.71$ (CHF). Lines denote the positive values of the second invariant of the velocity gradient tensor Q^+ (line contour levels are from 5×10^{-4} to 5×10^{-3} with an increment of 5×10^{-5}).

is intrinsically the same between the two thermal boundary conditions, whilst it is smaller than that (2.54) for U_b^+ (see also (1.14)). The resulting Reynolds analogy factor $2h_t/C_f = U_b^+/\theta_b^+$ or U_b^+/θ_m^+ is approximately 1.2 for $h^+ \approx 500$. Nearly the same value was obtained in a thermal boundary layer with air at low Reynolds number (Kong, Choi & Lee 2000; Li *et al.* 2009). The magnitude of $2h_t/C_f$ however tends to increase slowly with h^+ . To clarify the possible Pr effect, we have included the available DNS data for $Pr = 1$ (Hasegawa & Kasagi 2011; Pirozzoli *et al.* 2016) in figure 4(b). Whilst the magnitude of $2h_t/C_f$ becomes closer to unity for $Pr = 1$ at low Reynolds number, the slope remains invariably unchanged so that the difference becomes increasingly pronounced with h^+ . We infer that the difference in slope between U_b^+ and T_b^+ (or T_m^+) is associated with different characteristics in the overlap region between velocity and scalar fields, as will be seen below.

Figure 5 demonstrates that the relative contributions of the normalized values of $\langle \bar{\varepsilon}_\theta \rangle$ (or equivalently $\langle P_\theta \rangle$) and $\langle a(d\bar{\theta}/dy)^2 \rangle$ to T_m^+ (2.13) and T_b^+ (2.12). Clearly, the magnitude of $\langle \bar{\varepsilon}_\theta \rangle / U_\tau T_\tau^2$ increases logarithmically with increasing h^+ (figure 5a), while that of $\langle a(d\bar{\theta}/dy)^2 \rangle / U_\tau T_\tau^2$ is approximately constant (≈ 7.6 and 7.4 for CHF and CHS, respectively) for $h^+ \geq 400$ (figure 5b). As for $\langle \bar{\varepsilon} \rangle / U_\tau^3$ (see figure 3b of Abe & Antonia (2016)), the logarithmic h^+ increase for $\langle \bar{\varepsilon}_\theta \rangle / U_\tau T_\tau^2$ is established even at small h^+ (i.e. $h^+ \geq 400$), which is much lower than the Reynolds number for which the mean temperature log law holds. The latter reason is essentially associated with the overlap region of the mean turbulent scalar dissipation rate $\bar{\varepsilon}_\theta$ (see § 4.3). The logarithmic h^+ dependence of $\langle \bar{\varepsilon}_\theta \rangle / U_\tau T_\tau^2$ is represented well by

$$\langle \bar{\varepsilon}_\theta \rangle / U_\tau T_\tau^2 = 2.18 \ln(h^+) - C_\theta, \quad (4.6)$$

with $C_\theta = 5.2$ and 6.1 for CHF and CHS, respectively. Relation (4.6) was obtained by substituting the relations for T_m^+ (4.4) and T_b^+ (4.5) and the constants (7.6 and 7.4 for

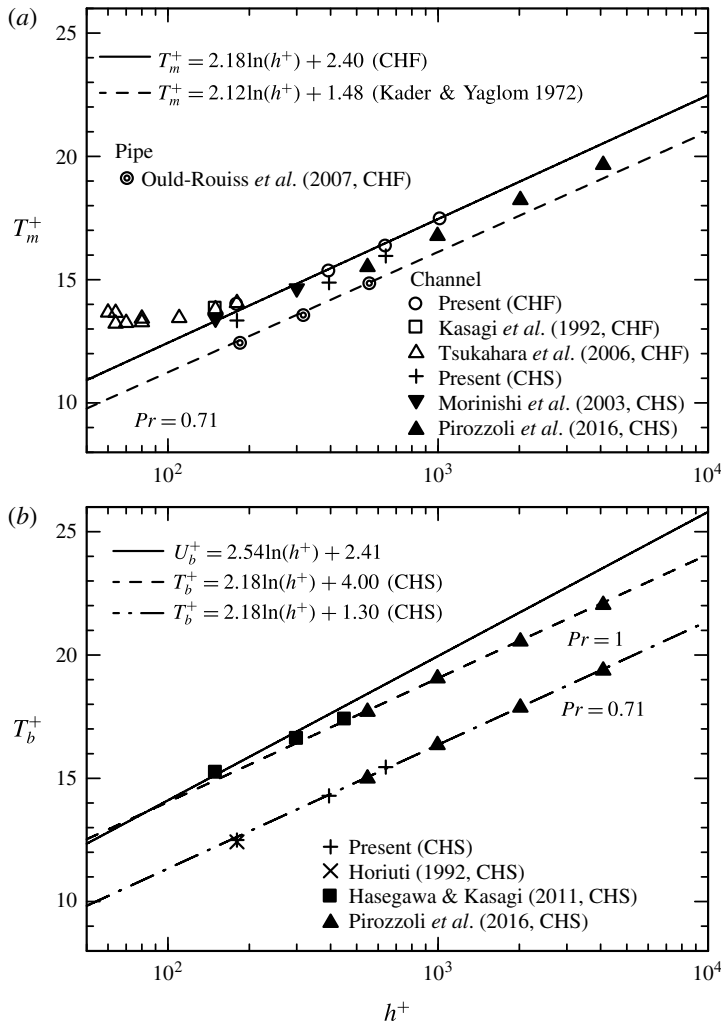


FIGURE 4. Distributions of T_m^+ and T_b^+ for $Pr = 0.71$ as a function of h^+ : (a) T_m^+ ; (b) T_b^+ .

CHF and CHS, respectively) of $\langle a(d\bar{\Theta}/dy)^2 \rangle / U_\tau T_\tau^2$ into (2.13) and (2.12). Viscosity affects $\langle \bar{\varepsilon}_\theta \rangle$ and $\langle a(d\bar{\Theta}/dy)^2 \rangle$ significantly below $h^+ = 400$ since there is no separation between the inner and outer regions.

We next discuss a possible relation for the heat transfer coefficient h_t (1.1), which may readily be obtained on the basis of a global energy balance by substituting the present T_m^+ relation (4.4) into (1.1), viz.

$$h_t = \frac{\sqrt{C_f/2}}{2.18 \ln(Re_b \sqrt{C_f/2\sqrt{2}}) + 2.40}. \quad (4.7)$$

Note that (4.7) is no longer analogous to (1.10), as derived by Kader & Yaglom (1972) from the log law since the latter is not assumed when obtaining (4.7). With the use of the logarithmic skin friction law (1.15), the present logarithmic heat transfer

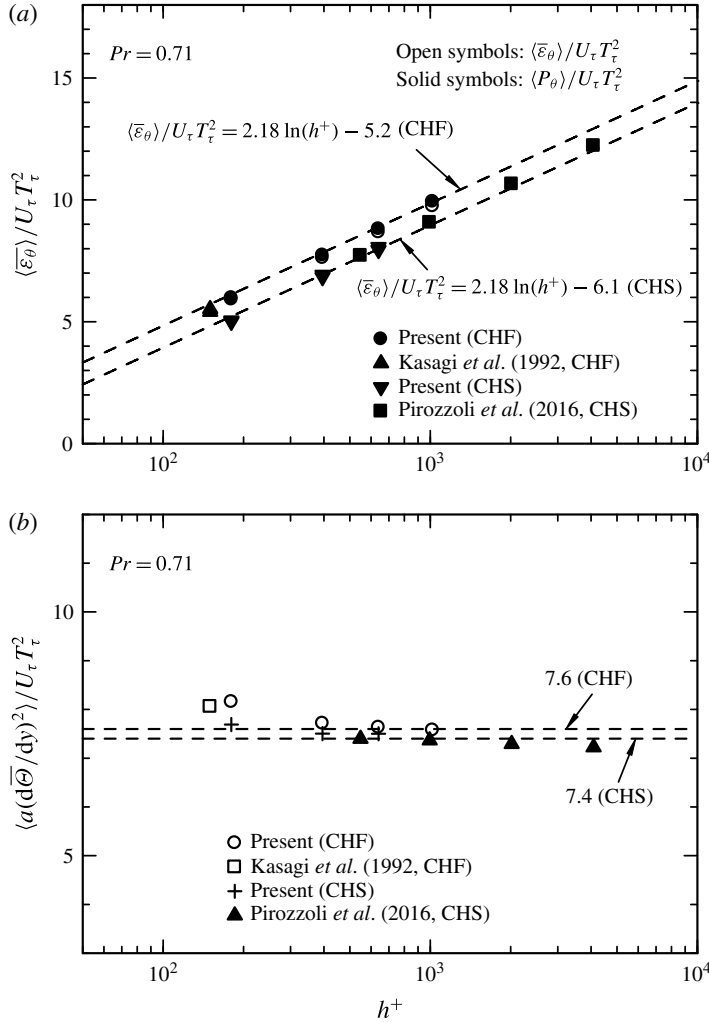


FIGURE 5. Distributions of $\langle \bar{\varepsilon}_\theta \rangle / U_\tau T_\tau^2$ and $\langle a(d\bar{\Theta}/dy)^2 \rangle / U_\tau T_\tau^2$ for $Pr = 0.71$ as a function of h^+ : (a) $\langle \bar{\varepsilon}_\theta \rangle / U_\tau T_\tau^2$; (b) $\langle a(d\bar{\Theta}/dy)^2 \rangle / U_\tau T_\tau^2$.

law (4.7) can then be used for evaluating the Reynolds number dependence of the Nusselt number, $Nu \equiv h_t Re_b Pr$. Figure 6 shows distributions of Nu for $Pr = 0.71$ with the DNS data for both CHF and CHS in the range $1.6 \times 10^3 \leq Re_b \leq 2.0 \times 10^5$ (i.e. $60 \leq h^+ \leq 4000$). This figure highlights that Nu obtained from both (4.7) and (1.15) gives a reasonable fit to the DNS data for CHF provided $Re_b \geq 6000$ (or equivalently $h^+ \geq 200$). On the other hand, since the constant heat flux is not guaranteed for CHS, the resulting Nu for CHS is a few per cent larger than that for CHF in the range $Re_b \geq 1.4 \times 10^4$ (or equivalently $h^+ \geq 400$) where T_m^+ also differs between the two thermal boundary conditions (see figure 4a). There is also a discernible difference between the present prediction and the well-known empirical relation obtained by Kays & Crawford (1980), i.e.

$$Nu = 0.021 Re_b^{0.8} Pr^{0.5}. \tag{4.8}$$

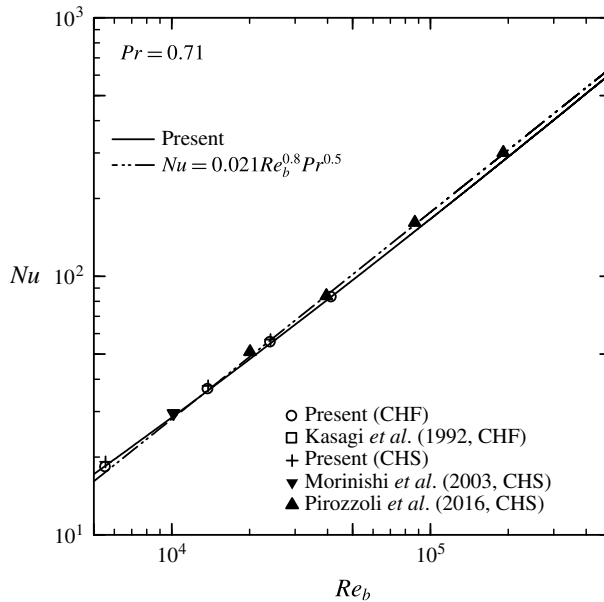


FIGURE 6. Distributions of Nu for $Pr = 0.71$ as a function of Re_b . Solid line represents the present relation obtained from both (4.7) and (1.15), whereas dashed line represents the empirical relation of Kays & Crawford (1980), $Nu = 0.021 Re_b^{0.8} Pr^{0.5}$.

This latter relation tends to overpredict the Nusselt number slightly in the range $Re_b \geq 1.4 \times 10^4$ and follow the DNS data for CHS. The lower h^+ bound of the present prediction for Nu (i.e. $h^+ \geq 200$) is approximately a factor of 2 smaller than that for T_m^+ ($h^+ \geq 400$). This is most likely due to the combined effect of the bulk mean velocity U_b^+ and the bulk mean scalar T_m^+ in the heat transfer coefficient h_t (i.e. equation (1.1)) since the logarithmic skin friction law is established on the basis of a global energy balance for $h^+ \geq 300$ (see Abe & Antonia 2016).

4.3. Scaling laws of $\overline{\varepsilon_\theta}$ and matching argument

In this subsection, we focus on the scaling of $\overline{\varepsilon_\theta}$ for $Pr = 0.71$ in the present flow to provide further insight into the logarithmic h^+ dependence of the integrated scalar dissipation $\langle \overline{\varepsilon_\theta} \rangle / U_\tau T_\tau^2$. The underlying idea of this analysis comes from the scaling arguments of Townsend (1976) (see § 8.8 of his book). Given that the effect of Pr on $\overline{\varepsilon_\theta}$ is confined near the wall (Na, Papavassiliou & Hanratty 1999; Kozuka et al. 2009; see also figure 6a), the inner and outer scaling laws may be written as

$$\overline{\varepsilon_\theta}^+ \equiv \overline{\varepsilon_\theta} \nu / U_\tau^2 T_\tau^2 = f(y^+, Pr) \tag{4.9}$$

and

$$\overline{\varepsilon_\theta} h / U_\tau T_\tau^2 = g(y/h), \tag{4.10}$$

respectively. While the magnitude of $\overline{\varepsilon_\theta}^+$ increases with h^+ close to the wall due to the effect of the inactive motion (Bradshaw 1967), $\overline{\varepsilon_\theta}^+$ seems to collapse for $y^+ \geq 30$ provided $h^+ \geq 400$ (figure 7). Viscous effects are unlikely to affect the turbulent scalar dissipation rate significantly for $y^+ > 30$. On the other hand, $\overline{\varepsilon_\theta}$ collapses

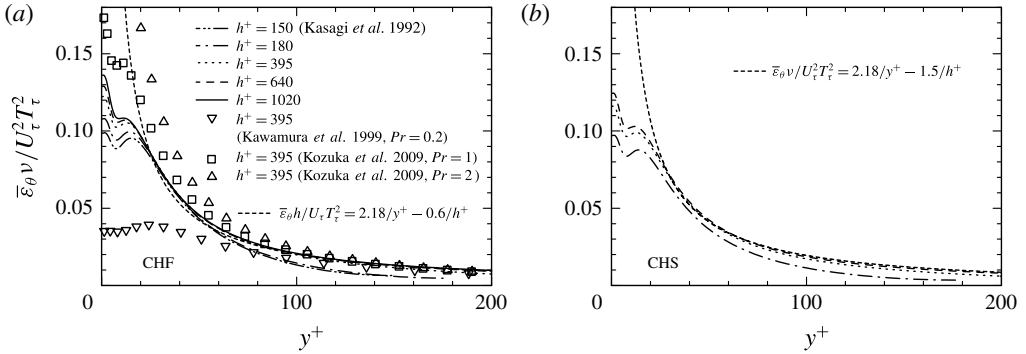


FIGURE 7. Distributions of $\bar{\epsilon}_\theta v / U_\tau^2 T_\tau^2$ for $Pr = 0.71$: (a) CHF; (b) CHS.

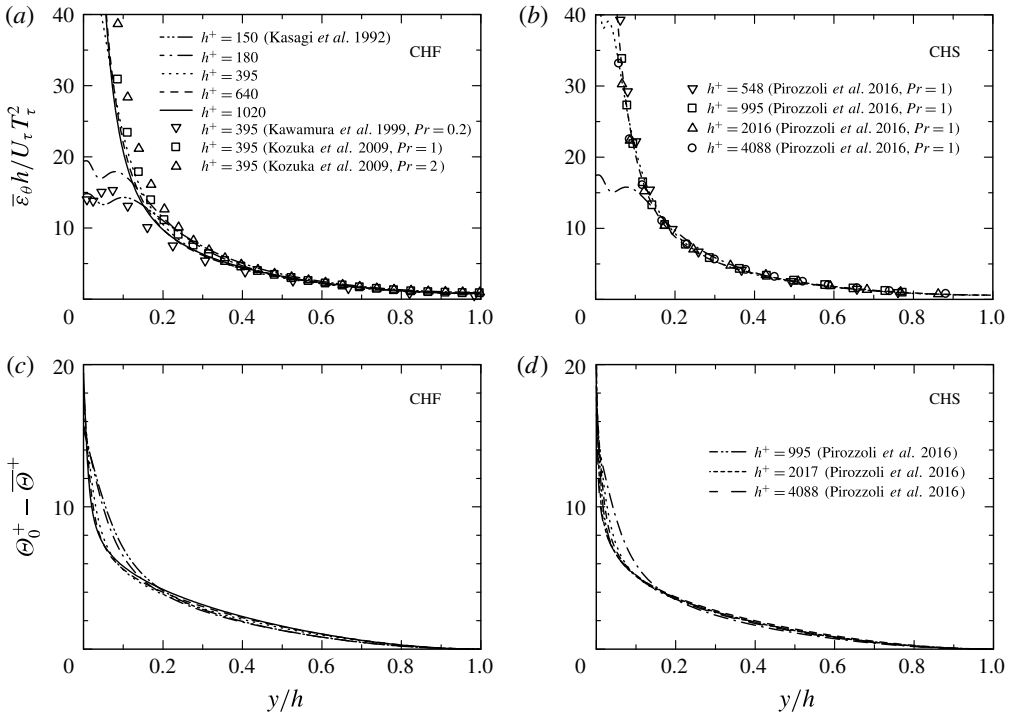


FIGURE 8. Distributions of $\bar{\epsilon}_\theta h / U_\tau T_\tau^2$ and $(\Theta_0 - \bar{\Theta}) / T_\tau$ for $Pr = 0.71$ as a function of h^+ : (a) $\bar{\epsilon}_\theta h / U_\tau T_\tau^2$ (CHF); (b) $\bar{\epsilon}_\theta h / U_\tau T_\tau^2$ (CHS); (c) $(\Theta_0 - \bar{\Theta}) / T_\tau$ (CHF); (d) $(\Theta_0 - \bar{\Theta}) / T_\tau$ (CHS).

almost perfectly on $U_\tau T_\tau^2$ and h in the region $30/h^+ < y/h < 1$ for $h^+ \geq 400$ (see figure 7a,b). The present results highlight that the outer layer similarity is more convincing for $\bar{\epsilon}_\theta$ than for $\bar{\Theta}$ even at small h^+ (see figure 8) as was observed for $\bar{\epsilon}$ by Abe & Antonia (2016).

We now apply a matching argument to $\bar{\epsilon}_\theta$. Here, we assume that h^+ is large enough to have a clear distinction between the inner and outer regions, and that there is a region where relations (4.9), (4.10) overlap so that the gradient of $\bar{\epsilon}_\theta$ should

coincide, viz.

$$\frac{d\bar{\varepsilon}_\theta}{dy} = \frac{U_\tau^3 T_\tau^2}{\nu^2} \frac{df}{dy^+} = \frac{U_\tau T_\tau^2}{h^2} \frac{dg}{dy^*}, \tag{4.11}$$

where $y^* \equiv y/h$. After multiplying by y^2 , the equality between the second and third members of (4.11) becomes

$$y^{+2} \frac{df}{dy^+} = y^{*2} \frac{dg}{dy^*}. \tag{4.12}$$

This is satisfied if

$$\frac{df}{dy^+} = \frac{D}{y^{+2}} \quad \text{or} \quad \frac{dg}{dy^*} = \frac{D}{y^{*2}}. \tag{4.13a,b}$$

Equation (4.12) indicates that $\bar{\varepsilon}_\theta$ should indeed scale on $U_\tau T_\tau^2$ and y in the overlap region. After integrating (4.13), we obtain

$$f = -\frac{D}{y^+} + D_1 \quad \text{or} \quad g = -\frac{D}{y^*} + D_2. \tag{4.14a,b}$$

Here, we adopt a small parameter $\gamma = 1/h^+$ and an outer variable $y^* = \gamma y^+$ as was done by Afzal (1976) for the mean velocity gradient. We then obtain $D_1 = -\gamma c_\theta$ and $D_2 = -c_\theta$ so that (4.14) is rewritten as

$$f = -\frac{D}{y^+} - \gamma c_\theta \quad \text{or} \quad \gamma g = -\gamma \frac{D}{y^*} - \gamma c_\theta, \tag{4.15a,b}$$

where c_θ is a constant. After normalization, it follows from (4.15) that the overlap scaling may be written as

$$\bar{\varepsilon}_\theta y / U_\tau T_\tau^2 = 1/\kappa_{\varepsilon\theta} - c_\theta (y^+ / h^+) \tag{4.16}$$

and

$$\bar{\varepsilon}_\theta y / U_\tau T_\tau^2 = 1/\kappa_{\varepsilon\theta} - c_\theta (y/h) \tag{4.17}$$

in inner and outer coordinates, respectively, where $D = -1/\kappa_{\varepsilon\theta}$ and $\kappa_{\varepsilon\theta}$ is a constant. Relations (4.16), (4.17) are analogous to those established for $\bar{\varepsilon}$ by Abe & Antonia (2016). The matching argument highlights that the overlap scaling of $\bar{\varepsilon}_\theta$ requires neither the existence of a scalar log law nor energy equilibrium ($P_\theta = \bar{\varepsilon}_\theta$). It does however require the Reynolds number to be large enough ($h^+ \approx 400$) to allow the overlap region, where the relevant length scale is y (the distance from the wall), to be distinguished unambiguously.

In (4.16), (4.17), the second terms of the right are responsible for the finite Reynolds number effect, i.e. $-c_\theta (y^+ / h^+)$ (the second term of (4.16)) goes to zero as $h^+ \rightarrow \infty$, while $-c_\theta (y/h)$ (the second term of (4.17)) does not depend on h^+ but may enhance the outer limit of the overlap scaling. A fit to the DNS data over $30/\delta^+ \leq y/\delta \leq 0.2$ then yields $1/\kappa_{\varepsilon\theta} = 2.18$ (viz. $\kappa_{\varepsilon\theta} = 0.46$) and $c_\theta = 0.6$ and 1.5 for CHF and CHS, respectively (see figure 9a,b). This finite Reynolds number effect comes from the effect of the mean pressure gradient, which is absent in a zero-pressure-gradient thermal boundary layer (Li *et al.* 2009). When the finite Reynolds number effect disappears ($h^+ \geq 5000$), equations (4.16) and (4.17) reduce to $\bar{\varepsilon}_\theta y / U_\tau T_\tau^2 = 1/\kappa_{\varepsilon\theta}$ analogous to the classical scaling based on the scalar log law $\bar{\varepsilon}_\theta y / U_\tau T_\tau^2 = 1/\kappa_\theta$ (see Abe & Antonia 2011).

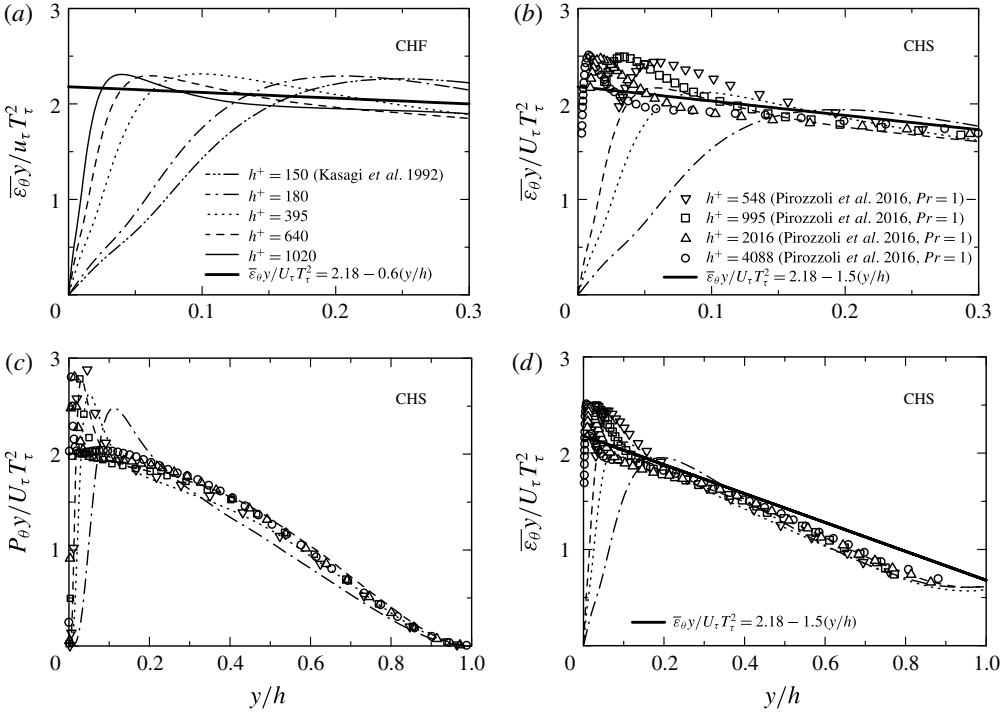


FIGURE 9. Distributions of $P_{\theta}y/U_{\tau}T_{\tau}^2$ and $\bar{\varepsilon}_{\theta}y/U_{\tau}T_{\tau}^2$ for $Pr=0.71$: (a) $\bar{\varepsilon}_{\theta}y/U_{\tau}T_{\tau}^2$ (CHF); (b) $\bar{\varepsilon}_{\theta}y/U_{\tau}T_{\tau}^2$ (CHS); (c) $P_{\theta}y/U_{\tau}T_{\tau}^2$ (CHS); (d) $\bar{\varepsilon}_{\theta}y/U_{\tau}T_{\tau}^2$ (CHS). Note that (b) is replotted in (d) with different scales to highlight the overlap scaling of P_{θ} and $\bar{\varepsilon}_{\theta}$.

A comparison between the normalized P_{θ} and $\bar{\varepsilon}_{\theta}$ (i.e. $P_{\theta}y/U_{\tau}T_{\tau}^2$ and $\bar{\varepsilon}_{\theta}y/U_{\tau}T_{\tau}^2$) may provide further insight into the overlap scaling for large and small scales. Figure 9(c,d) indicates that the collapse is more convincing for $\bar{\varepsilon}_{\theta}$ than for P_{θ} when h^{+} is larger than 400. This is because the log-law conditions for mean temperature (i.e. constant κ_{θ} and $\bar{v}\theta$) are required for the collapse of $P_{\theta}y/U_{\tau}T_{\tau}^2$, while the overlap scaling of $\bar{\varepsilon}_{\theta}$ only requires the Reynolds number to be large enough. The same trend is also observed for the relationship between the turbulent kinetic energy production P_k and the energy dissipation rate $\bar{\varepsilon}$ (see Abe & Antonia 2016). Note that $P_{\theta} = \bar{\varepsilon}_{\theta}$ does not hold strictly in the logarithmic and outer regions (see Pirozzoli *et al.* 2016) due to the presence of large-scale structures (see figure 3). This small departure from energy equilibrium however does not appear to affect the overlap scaling for $\bar{\Theta}$ significantly since it is difficult to distinguish κ_{θ} from $\kappa_{\varepsilon\theta}$ when the Reynolds number is sufficiently large (see figure 12). It would appear that the overlap region for the dissipation has indeed a higher rank than that for the mean field since the small scales (i.e. dissipation) are likely to ‘lose’ their dependence on the Reynolds number more rapidly than the large scales (i.e. the mean field).

Note that (4.16), (4.17) represent the outer scaling in a wider range of the y location than expected, *viz.*

$$\bar{\varepsilon}_{\theta}h/U_{\tau}T_{\tau}^2 = 2.18/(y/h) - c_{\theta} \tag{4.18}$$

(see figure 10). In particular, there is excellent collapse of (4.18) for CHS up to the centreline (see figure 10b), consistent with a smaller departure from the mean scalar

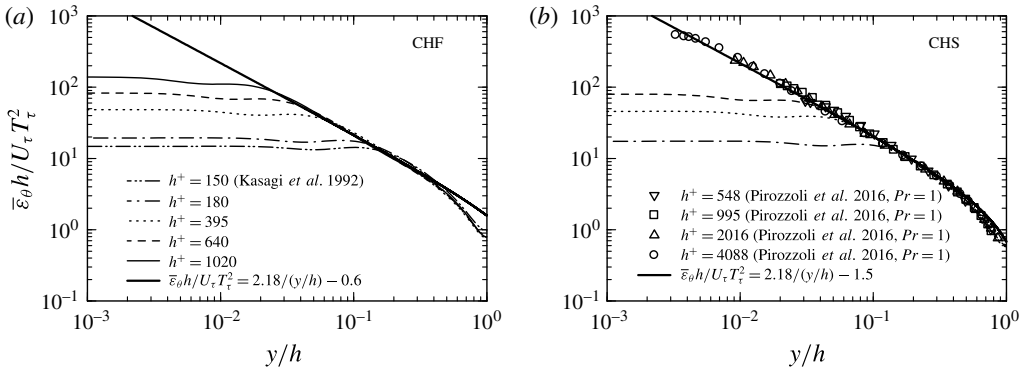


FIGURE 10. Distributions of $\bar{\varepsilon}_\theta h / U_\tau T_\tau^2$ for $Pr = 0.71$ with log–log coordinates: (a) CHF; (b) CHS.

log law (see figure 12c where $1/\kappa_\theta \equiv y^+(d\bar{\Theta}^+/dy^+)$ is plotted). This underlines the existence of a large overlap region for $\bar{\varepsilon}_\theta$ at $Pr = 0.71$, as was observed for $\bar{\Theta}$.

4.4. Fractional contributions to $\langle \bar{\varepsilon}_\theta \rangle / U_\tau T_\tau^2$

It is of importance to clarify if the integral of $\bar{\varepsilon}_\theta$ over the overlap region yields the logarithmic h^+ dependence of $\langle \bar{\varepsilon}_\theta \rangle / U_\tau T_\tau^2$. In the present study, we follow the same approach as in Sreenivasan (1995) and Abe & Antonia (2016) for $\langle \bar{\varepsilon} \rangle / U_\tau^3$, viz.

$$\frac{\langle \bar{\varepsilon}_\theta \rangle}{U_\tau T_\tau^2} = \underbrace{\int_0^{30} \bar{\varepsilon}_\theta^+ dy^+}_{C_i} + \underbrace{\int_{30\nu/U_\tau}^{0.2h} \frac{\bar{\varepsilon}_\theta}{U_\tau T_\tau^2} dy}_{C_{log}} + \underbrace{\int_{0.2}^1 \frac{\bar{\varepsilon}_\theta h}{U_\tau T_\tau^2} d\left(\frac{y}{h}\right)}_{C_o}, \quad (4.19)$$

where the limits for the second integral in (4.19) correspond to the extent of the overlap region of $\bar{\varepsilon}_\theta$ for $Pr = 0.71$ (i.e. from $y^+ \simeq 30$ to $y/h = 0.2$). Values of C_i , C_{log} and C_o obtained from the present DNS data are shown in figure 11. Also included in this figure are the C_{log} and C_o data of Pirozzoli et al. (2016) for $Pr = 1$ since the outer layer similarity is convincing for $\bar{\varepsilon}_\theta h / U_\tau T_\tau^2$ (see figure 8b). Clearly, there is a $\ln(h^+)$ dependence for C_{log} . This dependence is obtained by integrating (4.16) or (4.17), viz.

$$C_{log} \simeq \int_{30\nu/U_\tau}^{0.2h} \left(\frac{1}{\kappa_\theta y} - \frac{c_\theta}{h} \right) dy = 2.18(\ln(h^+) + \ln(0.2) - \ln(30)) - c_\theta(0.2 - 30/h^+), \quad (4.20)$$

in which the last term of (4.20), the finite Reynolds number effect, cannot be dismissed when h^+ is small. Given that C_o is essentially constant but the magnitude of C_i increases slowly with h^+ (figure 11), we integrate $\bar{\varepsilon}_\theta$ from $y = 0$ to $0.2h$ (viz. $C_i + C_{log}$). The resulting integral is described adequately by

$$C_i + C_{log} = \int_0^{0.2h} \frac{\langle \bar{\varepsilon}_\theta \rangle}{U_\tau T_\tau^2} dy = 2.18 \ln(h^+) - C_2 \quad (4.21)$$

for $h^+ \geq 400$ with $C_2 = 7.7$ and 8.2 for CHF and CHS, respectively. Note that the sum of (4.21) and C_o ((2.5) and (2.1) for CHF and CHS, respectively) is identical to (4.6).

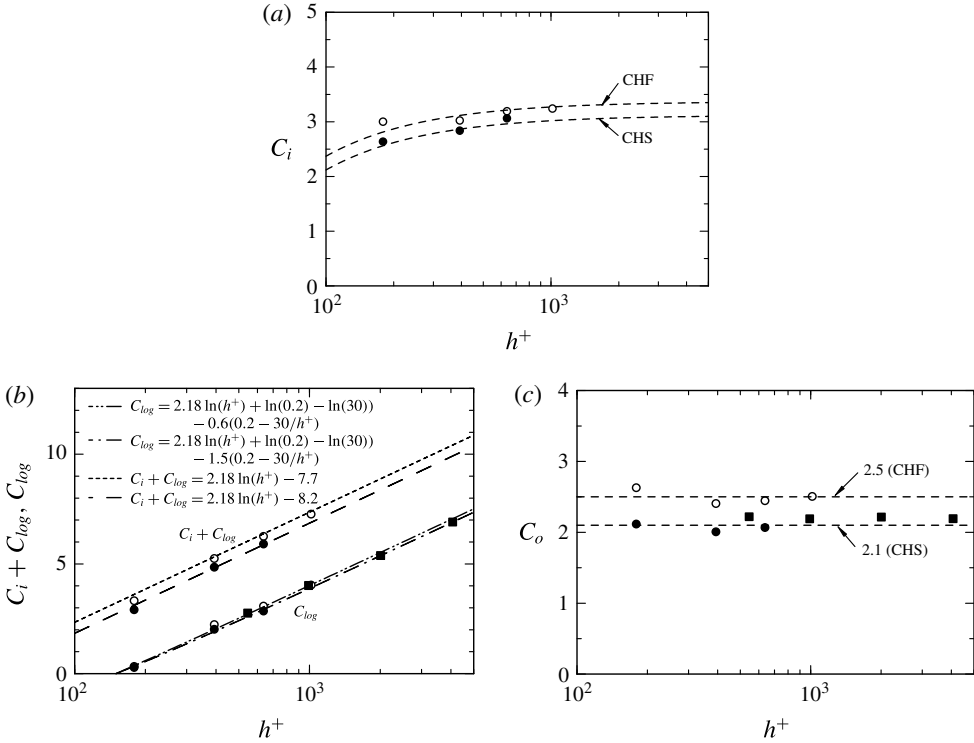


FIGURE 11. Distributions of piecewise contributions to $\langle \bar{\varepsilon}_\theta \rangle / U_\tau T_\tau^2$ for $Pr = 0.71$ as a function of h^+ : (a) from $y^+ = 0$ to 30 (C_i); (b) from $y^+ = 30$ to $y/\delta = 0.2$ (C_{log}) and from $y/\delta = 0$ to 0.2 ($C_i + C_{log}$); (c) from $y/\delta = 0.2$ to 1 (C_o). \circ , Present (CHF); \bullet , Present (CHS); \blacksquare , Pirozzoli *et al.* (2016) for $Pr = 1$.

This implies that the more appropriate expression for the logarithmic dependence of $\langle \bar{\varepsilon}_\theta \rangle / U_\tau T_\tau^2$ for the channel requires integration from $y=0$ to $0.2h$, *viz.* the contribution of C_i (h^+) cannot be ignored. The present results highlight that the slope of 2.18 in (4.21) can be identified with $1/\kappa_{\varepsilon\theta}$ as inferred from the overlap scaling of $\bar{\varepsilon}_\theta$, and that $1/\kappa_{\varepsilon\theta}$ is identical with the slope for the $\ln(h^+)$ dependence of the integrated mean scalar.

When $h^+ \rightarrow \infty$, the overlap region should contribute exclusively to the $2.18 \ln(h^+)$ dependence of the integrated turbulent scalar energy dissipation rate. The present logarithmic h^+ dependence of T_b^+ and T_m^+ for CHS and CHF, respectively, is essentially linked to the excellent overlap region we observe for $\bar{\varepsilon}_\theta$ even at small h^+ . Note that $\kappa_{\varepsilon\theta} = 0.46$ defined in (4.16), (4.17) is not identical with κ_θ obtained from the scalar log law (4.1) for the Reynolds numbers examined (see figure 12). This is because, as for the mean velocity (see McKeon & Morrison 2007, Smits, McKeon & Marusic 2011), the constancy of $1/\kappa_\theta \equiv y^+(d\bar{\theta}^+/dy^+)$ is most likely to be established beyond $h^+ = 5000$ (see figure 12b) due to the non-negligible viscous effect (note that no collapse of the data is observed for $h^+ = 180$ due to the low Re effects). Figure 12 highlights the slow increase of κ_θ with increasing h^+ , *i.e.* $\kappa_\theta = 0.40$ for $h^+ = 395$ (CHF) (Kawamura *et al.* 1999), $\kappa_\theta = 0.43$ for $h^+ = 1020$ (CHF) (Abe *et al.* 2004a) and $\kappa_\theta = 0.46$ for $h^+ = 4088$ (CHS) (Pirozzoli *et al.* 2016). Pirozzoli *et al.* (2016) inferred $\kappa_\theta = 0.46$ as the high Re asymptotic value on the basis of

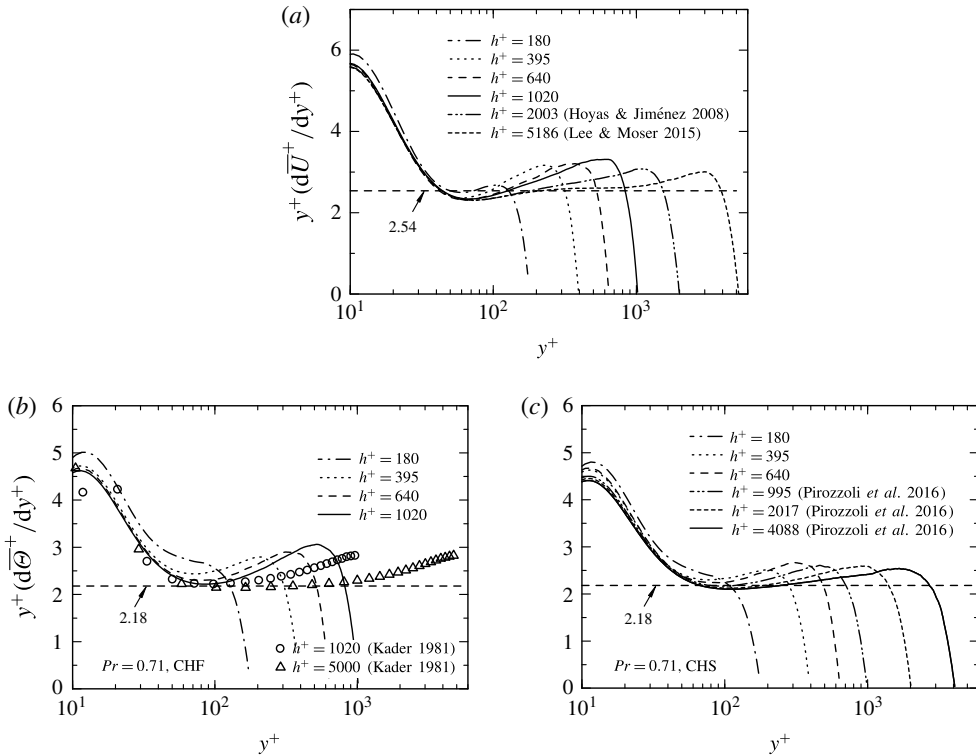


FIGURE 12. Distributions of $y^+(d\bar{U}^+/dy^+)$ and $y^+(d\bar{\Theta}^+/dy^+)$ for $Pr = 0.71$: (a) $y^+(d\bar{U}^+/dy^+)$; (b) $y^+(d\bar{\Theta}^+/dy^+)$ (CHF); (c) $y^+(d\bar{\Theta}^+/dy^+)$ (CHS).

their datasets for the CHS case. Note that the departure from the scalar log law is smaller for CHS than for CHF due to the smaller magnitude of the mean scalar gradient, as discussed in §4.1. Figure 12 also demonstrates that values of κ and κ_θ have most likely converged to different values (*viz.* $\kappa = 0.39$ and $\kappa_\theta = 0.46$) at large Reynolds numbers, where the ratio $\kappa/\kappa_\theta \approx 0.85$ corresponds to the magnitude of Pr_t in the logarithmic region (see figure 2b). Marusic *et al.* (2013) reported $\kappa = 0.39$ in a laboratory boundary layer, pipe and atmospheric surface layer. Kader & Yaglom (1972) also analysed the experimental data in a channel, pipe and boundary layer for a wide range of the Reynolds number and concluded $\kappa_\theta = 0.47$. Subramanian & Antonia (1981) also reported $\kappa_\theta = 0.48 \pm 0.02$ in a laboratory thermal boundary layer. The present value of $\kappa_{\varepsilon\theta} = 0.46$ may be reconcilable with the value of κ_θ (obtained at very large h^+) if one recognizes that the outer layer similarity of $\bar{\varepsilon}_\theta$ is established at a much smaller h^+ than for $\bar{\Theta}^+$. Indeed, this appears to be adequately supported by the available DNS data (see figure 8).

5. Conclusions

The integration of mean and turbulent scalar dissipation rates across half the channel (which is equivalent to performing a global energy balance) has been carried out using the present DNS datasets (up to $h^+ = 1000$) in a fully developed turbulent channel flow with passive scalar transport for $Pr = 0.71$. The results are compared with those

obtained from existing DNS datasets up to $h^+ = 4000$. Two isothermal conditions (i.e. CHS and CHF) have been examined. After clarifying the difference between these conditions, unambiguous relations for the dependence of T_b^+ (CHS) and T_m^+ (CHF) on h^+ have been obtained based on the energy balances for both the mean and turbulent scalar variance. The scaling behaviour of the turbulent scalar dissipation rate has also been carefully examined in order to confirm the logarithmic dependence of T_b^+ and T_m^+ on h^+ . The main conclusions are as follows.

After normalizing by $U_\tau T_\tau^2$, the scalar dissipation function, or sum of the integrals of the mean and turbulent scalar dissipation rates, is equal to T_b^+ and T_m^+ (i.e. equations (2.12)–(2.13)) for CHS and CHF, respectively. The logarithmic h^+ dependence is established quite well (i.e. with significant confidence and minimal ambiguity) for the integrated mean scalar provided $h^+ \geq 400$ where the integral of the mean scalar dissipation rate associated with the mean scalar gradient, i.e. $\langle a(d\bar{\theta}/dy)^2 \rangle$, normalized by $U_\tau T_\tau^2$, is essentially constant, whereas $\langle \bar{\varepsilon}_\theta \rangle / U_\tau T_\tau^2$ increases logarithmically with increasing h^+ . Viscosity affects $\langle a(d\bar{\theta}/dy)^2 \rangle / U_\tau T_\tau^2$ significantly for $h^+ < 400$. The logarithmic h^+ dependence of $\langle \bar{\varepsilon}_\theta \rangle / U_\tau T_\tau^2$ is hence linked to that of T_b^+ or T_m^+ . The resulting relation for the heat transfer coefficient (4.7) is supported convincingly by the DNS data for CHF in the range $h^+ \geq 200$. The lower h^+ bound of (4.7) is about by a factor of 3 smaller than that of (1.10) derived by Kader & Yaglom (1972) from the log law in a pipe flow.

Support for the logarithmic h^+ dependence of $\langle \bar{\varepsilon}_\theta \rangle / U_\tau T_\tau^2$ is provided by the scaling behaviour of the mean turbulent scalar dissipation rate. The inner layer scaling, i.e. $\bar{\varepsilon}_\theta \nu / U_\tau^2 T_\tau^2 = f(y^+, Pr)$, does not hold for $y^+ \leq 30$. On the other hand, $\bar{\varepsilon}_\theta$ collapses almost perfectly with $U_\tau T_\tau^2$ and h in the region $30/h^+ < y/h < 1$. Unlike the mean scalar, the turbulent scalar dissipation rate is not affected significantly by viscosity for $y^+ > 30$. Whereas the classical overlap argument based on $\bar{\theta}$ strictly holds only at large h^+ (Monin & Yaglom 1971; Kader 1981), the overlap region for $\bar{\varepsilon}_\theta$ is established at small h^+ (≈ 400) independently of the existence of a scalar log law. It does however require the Reynolds number to be large enough ($h^+ \approx 400$) to allow an overlap region where the relevant length scale is y . In this region ($30/h^+ \leq y/h \leq 0.2$), $\bar{\varepsilon}_\theta y / U_\tau T_\tau^2$ approaches a constant ($\kappa_{\varepsilon\theta}^{-1} = 2.18$), allowing for a finite Reynolds number correction, equations (4.16), (4.17), for $h^+ \geq 400$. When h^+ is sufficiently large (≥ 5000) (see figure 12b) for the scalar log law to be established over a region where $P_\theta \simeq \bar{\varepsilon}_\theta$ and $-\bar{v}\bar{\theta} \simeq \text{constant}$, the von Kármán constant for the mean scalar $\kappa_\theta = 0.46$ can be identified with $\kappa_{\varepsilon\theta}$; the ratio $\kappa/\kappa_\theta \approx 0.85$ corresponds to the value of Pr_t in the overlap region. The enhanced scalar transport by vortical motions is also responsible for the decrease of Pr_t towards the centreline. The present logarithmic h^+ dependence of T_b^+ and T_m^+ follows from the overlap argument based entirely on the behaviour of $\bar{\varepsilon}_\theta$ in the inner and outer regions. We stress that the outer layer similarity of $\bar{\varepsilon}_\theta$ is more convincing than that of $\bar{\theta}$ and is established at a smaller value of h^+ (see figure 8). This is the reason why the present T_b^+ and T_m^+ relations (4.5), (4.4) are validated over a wide range of h^+ and are established at a lower Reynolds number than the mean temperature log law.

The establishment of the slopes for the logarithmic skin friction law (i.e. 2.54) (see Abe & Antonia 2016) and heat transfer law (i.e. 2.18) at small h^+ is an important outcome resulting from the present approach, *viz.* the use of the global energy budget, since these slopes are intrinsically associated with the ‘asymptotic’ values of the log-law slopes even though the mean velocity and mean temperature have yet to reach their asymptotic state.

Acknowledgements

Computations performed on the JAXA (Japan Aerospace Exploration Agency) Supercomputer System are gratefully acknowledged. H.A. is grateful to Professor H. Kawamura and Dr Y. Matsuo for earlier collaborations.

REFERENCES

- ABE, H. & ANTONIA, R. A. 2009 Turbulent Prandtl number in a channel flow for $Pr = 0.025$ and 0.71 . In *Proceedings of the 6th International Symposium on Turbulence and Shear Flow Phenomena, Seoul, Korea* (ed. N. Kasagi, J. K. Eaton, R. Friedrich, J. A. C. Humphrey, A. V. Johansson & H. J. Sung), vol. 1, pp. 67–72.
- ABE, H. & ANTONIA, R. A. 2011 Scaling of normalized mean energy and scalar dissipation rates in a turbulent channel flow. *Phys. Fluids* **23**, 055104.
- ABE, H. & ANTONIA, R. A. 2016 Relationship between the energy dissipation function and the skin friction law in a turbulent channel flow. *J. Fluid Mech.* **798**, 140–164.
- ABE, H., ANTONIA, R. A. & KAWAMURA, H. 2009 Correlation between small-scale velocity and scalar fluctuations in a turbulent channel flow. *J. Fluid Mech.* **627**, 1–32.
- ABE, H., KAWAMURA, H. & CHOI, H. 2004b Very large-scale structures and their effects on the wall shear-stress fluctuations in a turbulent channel flow up to $Re_\tau = 640$. *Trans. ASME J. Fluids Engng* **126**, 835–843.
- ABE, H., KAWAMURA, H. & MATSUO, Y. 2001 Direct numerical simulation of a fully developed turbulent channel flow with respect to the Reynolds number dependence. *Trans. ASME J. Fluids Engng* **123**, 382–393.
- ABE, H., KAWAMURA, H. & MATSUO, Y. 2004a Surface heat-flux fluctuations in a turbulent channel flow up to $Re_\tau = 1020$ with $Pr = 0.025$ and 0.71 . *Intl J. Heat Fluid Flow* **25**, 404–419.
- AFZAL, N. 1976 Millikan's argument at moderately large Reynolds number. *Phys. Fluids* **19**, 600–602.
- ANTONIA, R. A., ABE, H. & KAWAMURA, H. 2009 Analogy between velocity and scalar fields in a turbulent channel flow. *J. Fluid Mech.* **628**, 241–268.
- BERNARDINI, M., PIROZZOLI, S. & ORLANDI, P. 2014 Velocity statistics in turbulent channel flow up to $Re_\tau = 4000$. *J. Fluid Mech.* **742**, 171–191.
- BRADSHAW, B. 1967 'Inactive' motion and pressure fluctuations in turbulent boundary layers. *J. Fluid Mech.* **30**, 241–258.
- DEAN, R. B. 1978 Reynolds number dependence of skin friction and other bulk flow variables in two-dimensional rectangular duct flow. *Trans. ASME J. Fluids Engng* **100**, 215–223.
- DJENIDI, L. & ANTONIA, R. A. 2009 Momentum and heat transport in a three-dimensional transitional wake of a heated square cylinder. *J. Fluid Mech.* **640**, 109–129.
- GUEZENNEC, Y., STRETCH, D. & KIM, J. 1990 The structure of turbulent channel flow with passive scalar transport. In *Proceedings of the Summer Program 1990*, pp. 127–138. Centre for Turbulence Research, Stanford University.
- HASEGAWA, Y. & KASAGI, N. 2011 Dissimilar control of momentum and heat transfer in a fully developed turbulent channel flow. *J. Fluid Mech.* **683**, 57–93.
- HORIUTI, K. 1992 Assessment of two-equation models of turbulent passive-scalar diffusion in channel flow. *J. Fluid Mech.* **238**, 405–433.
- HOYAS, S. & JIMÉNEZ, J. 2008 Reynolds number effects on the Reynolds-stress budgets in turbulent channels. *Phys. Fluids* **20**, 101511.
- JOHANSSON, A. V. & WIKSTRÖM, P. M. 1999 DNS and modelling of passive scalar transport in turbulent channel flow with a focus on scalar dissipation rate modelling. *Flow Turbul. Combust.* **63**, 223–245.
- KADER, B. A. 1981 Temperature and concentration profiles in fully turbulent boundary layers. *Intl J. Heat Mass Transfer* **24**, 1541–1544.
- KADER, B. A. & YAGLOM, A. M. 1972 Heat and mass transfer laws for fully turbulent wall flows. *Intl. J. Heat Mass Transfer* **15**, 2329–2351.

- KANEDA, Y., MORISHITA, K. & ISHIHARA, T. 2013 Small scale universality and spectral characteristics in turbulent flows. In *Proceedings of the 8th International Symposium on Turbulence and Shear Flow Phenomena, Poitiers, France (INV2)*.
- KASAGI, N., TOMITA, Y. & KURODA, A. 1992 Direct numerical simulation of passive scalar field in a turbulent channel flow. *Trans. ASME J. Heat Transfer* **114**, 598–606.
- KAWAMURA, H., ABE, H. & MATSUO, Y. 1999 DNS of turbulent heat transfer in channel flow with respect to Reynolds and Prandtl number effects. *Intl J. Heat Fluid Flow* **20**, 196–207.
- KAYS, W. M. 1966 *Convective Heat and Mass Transfer*. McGraw-Hill.
- KAYS, W. M. & CRAWFORD, M. E. 1980 *Convective Heat and Mass Transfer*, 2nd edn. McGraw-Hill.
- KIM, J. & MOIN, P. 1989 Transport of passive scalars in a turbulent channel flow. In *Turbulent Shear Flows* (ed. J.-C. André, J. Cousteix, F. Durst, B. E. Launder, F. W. Schmidt & J. H. Whitelaw), vol. 6, pp. 85–96. Springer.
- KONG, H., CHOI, H. & LEE, J. S. 2000 Direct numerical simulation of turbulent thermal boundary layers. *Phys. Fluids* **12**, 2555–2568.
- KOZUKA, M., SEKI, Y. & KAWAMURA, H. 2009 DNS of turbulent heat transfer in a channel flow with a high spatial resolution. *Intl J. Heat Fluid Flow* **30**, 514–524.
- LEE, M. & MOSER, R. D. 2015 Direct numerical simulation of turbulent channel flow up to $Re_\tau \approx 5200$. *J. Fluid Mech.* **774**, 395–415.
- LI, Q., SCHLATTER, P., BRANDT, L. & HENNINGSON, D. S. 2009 DNS of a spatially developing turbulent boundary layer with passive scalar transport. *Intl J. Heat Fluid Flow* **30**, 916–929.
- LOZANO-DURÁN, A. & JIMÉNEZ, J. 2014 Effect of the computational domain on direct simulations of turbulent channels up to $Re_\tau = 4200$. *Phys. Fluids* **26**, 011702.
- LYONS, S. L., HANRATTY, T. J. & MCLAUGHLIN, J. B. 1991 Direct numerical simulation of passive heat transfer in a turbulent channel flow. *Intl J. Heat Mass Transfer* **34**, 1149–1161.
- MARUSIC, I., MONTY, J. P., HULTMARK, M. & SMITS, A. J. 2013 On the logarithmic region in wall turbulence. *J. Fluid Mech.* **716**, R3.
- MCKEON, B. J. & MORRISON, J. F. 2007 Asymptotic scaling in turbulent pipe flow. *Phil. Trans. R. Soc. Lond. A* **365**, 771–787.
- MONIN, A. S. & YAGLOM, A. M. 1971 *Statistical Fluid Mechanics: Mechanics of Turbulence*, vol. 1. MIT Press.
- MONTY, J. P. 2005 Developments in smooth wall turbulent duct flows. PhD thesis, University of Melbourne, Australia.
- MORINISHI, Y., LUND, T. S., VASILYEV, O. V. & MOIN, P. 1998 Fully conservative higher order finite difference schemes for incompressible flow. *J. Comput. Phys.* **143**, 90–124.
- MORINISHI, Y., TAMANO, S. & NAKAMURA, E. 2003 Numerical analysis of incompressible turbulent channel flow with different thermal wall boundary conditions. *Trans. JSME B* **69**, 1313–1320; (in Japanese).
- NA, Y., PAPAVALIIOU, D. V. & HANRATTY, T. J. 1999 Use of direct numerical simulation to study the effect of Prandtl number on temperature fields. *Intl J. Heat Fluid Flow* **20**, 187–195.
- NAGANO, Y. & KIM, C. 1988 A two-equation model for heat transport in wall turbulent shear flows. *Trans. ASME J. Heat Transfer* **110**, 583–589.
- NAGANO, Y. & TAGAWA, M. 1988 Statistical characteristics of wall turbulence with a passive scalar. *J. Fluid Mech.* **196**, 157–185.
- OULD-ROUÏSS, M., BOUSBAI, M. & MAZOUZ, A. 2013 Large eddy simulation of turbulent heat transfer in pipe flows with respect to Reynolds and Prandtl number effects. *Acta Mechanica* **224**, 1133–1155.
- PIROZZOLI, S., BERNARDINI, M. & ORLANDI, P. 2016 Passive scalars in turbulent channel flow at high Reynolds number. *J. Fluid Mech.* **788**, 614–639.
- ROGERS, M. M., MANSOUR, N. N. & REYNOLDS, W. C. 1989 An algebraic model for the turbulent flux of a passive scalar. *J. Fluid Mech.* **203**, 77–101.
- ROTTA, J. C. 1962 Turbulent boundary layers in incompressible flow. *Prog. Aeronaut. Sci.* **2**, 1–219.
- SARUWATARI, S. & YAMAMOTO, Y. 2014 Prandtl number effect on near wall temperature profile in high-Reynolds number channel flows. *Trans. JSME B* **80** (814), 20p (in Japanese).

- SEKI, Y., ABE, H. & KAWAMURA, H. 2003 DNS of turbulent heat transfer in a channel flow with different thermal boundary conditions. In *Proceedings of the 6th ASME-JSME Thermal Engineering Joint Conference, March 16–20, TED-AJ03-226*.
- SIMPSON, R. L., WHITTEN, D. G. & MOFFAT, R. J. 1970 An experimental study of the turbulent Prandtl number of air with injection and suction. *Intl J. Heat Mass Transfer* **13**, 125–143.
- SMITS, A. J., MCKEON, B. J. & MARUSIC, I. 2011 High-Reynolds number wall turbulence. *Annu. Rev. Fluid Mech.* **43**, 353–375.
- SREENIVASAN, K. R. 1995 The energy dissipation in turbulent shear flows. In *Symposium on Developments in Fluid Dynamics and Aerospace Engineering* (ed. S. M. Deshpande, A. Prabhu, K. R. Sreenivasan & P. R. Viswanath), pp. 159–190. Interline.
- SUBRAMANIAN, C. S. & ANTONIA, R. A. 1981 Effect of Reynolds number on a slightly heated turbulent boundary layer. *Intl J. Heat Mass Transfer* **24** (11), 1833–1846.
- TEITEL, M. & ANTONIA, R. A. 1993 Heat transfer in a fully developed turbulent channel flow: comparison between experiment and direct numerical simulations. *Intl J. Heat Mass Transfer* **36** (6), 1701–1706.
- TOWNSEND, A. A. 1976 *The Structure of Turbulent Shear Flow*, vol. 2. Cambridge University Press.
- TSUKAHARA, T., IWAMOTO, K., KAWAMURA, H. & TAKEDA, T. 2006 DNS of heat transfer in a transitional channel flow accompanied by a turbulent puff-like structure. In *Proceedings of Turbulence, Heat and Mass Transfer Conference 5, Dubrovnik, Croatia*, pp. 193–196. Begell House.
- ZANOUN, E.-S., DURST, F. & NAGIB, H. 2003 Evaluating the law of the wall in two-dimensional fully developed turbulent channel flows. *Phys. Fluids* **15**, 3079–3089.
- ZANOUN, E.-S., NAGIB, H. & DURST, F. 2009 Refined C_f relation for turbulent channels and consequences for high Re experiments. *Fluid Dyn. Res.* **41**, 1–12.